

# Do topology and ferromagnetism cooperate at the EuS/Bi<sub>2</sub>Se<sub>3</sub> interface?

J. A. Krieger,<sup>1,2,3,\*</sup> Y. Ou,<sup>4</sup> M. Caputo,<sup>2</sup> A. Chikina,<sup>2</sup> M. Döbeli,<sup>5</sup> M.-A. Husanu,<sup>2,6</sup> I. Keren,<sup>1</sup> T. Prokscha,<sup>1</sup> A. Suter,<sup>1</sup> C.-Z. Chang,<sup>4,7</sup> J. S. Moodera,<sup>4,8</sup> V. N. Strocov,<sup>2,†</sup> and Z. Salman<sup>1,‡</sup>

<sup>1</sup>Laboratory for Muon Spin Spectroscopy, Paul Scherrer Institute, CH-5232 Villigen PSI, Switzerland

<sup>2</sup>Swiss Light Source, Paul Scherrer Institute, CH-5232 Villigen PSI, Switzerland

<sup>3</sup>Laboratorium für Festkörperphysik, ETH Zürich, CH-8093 Zürich, Switzerland

<sup>4</sup>Francis Bitter Magnet Lab, Massachusetts Institute of Technology, Cambridge, Massachusetts 02139, USA

<sup>5</sup>Ion Beam Physics, ETH Zürich, Otto-Stern-Weg 5, CH-8093 Zürich, Switzerland

<sup>6</sup>National Institute of Materials Physics, Atomistilor 405A, 077125 Magurele, Romania

<sup>7</sup>Department of Physics, The Penn State University, State College, Pennsylvania 16802, USA

<sup>8</sup>Department of Physics, Massachusetts Institute of Technology, Cambridge, Massachusetts 02139, USA

(Dated: February 9, 2022)

We probe the local magnetic properties of interfaces between the insulating ferromagnet EuS and the topological insulator Bi<sub>2</sub>Se<sub>3</sub> using low energy muon spin rotation (LE- $\mu$ SR). We compare these to the interface between EuS and the topologically trivial metal, titanium. Below the magnetic transition of EuS, we detect strong local magnetic fields which extend several nm into the adjacent layer and cause a complete depolarization of the muons. However, in both Bi<sub>2</sub>Se<sub>3</sub> and titanium we measure similar local magnetic fields, implying that their origin is mostly independent of the topological properties of the interface electronic states. In addition, we use resonant soft X-ray angle resolved photoemission spectroscopy (SX-ARPES) to probe the electronic band structure at the interface between EuS and Bi<sub>2</sub>Se<sub>3</sub>. By tuning the photon energy to the Eu anti-resonance at the Eu  $M_5$  pre-edge we are able to detect the Bi<sub>2</sub>Se<sub>3</sub> conduction band, through a protective Al<sub>2</sub>O<sub>3</sub> capping layer and the EuS layer. Moreover, we observe a signature of an interface-induced modification of the buried Bi<sub>2</sub>Se<sub>3</sub> wave functions and/or the presence of interface states.

## INTRODUCTION

Breaking the time reversal symmetry in topological insulators (TI) opens a gap in the topological surface states (TSS) which are otherwise protected against local perturbations. This has been proposed as a route towards several new quantum phenomena, such as the quantum anomalous Hall (QAH) effect [1], the topological magneto-electric effect [2] and even Majorana excitations, when in proximity to an  $s$ -wave superconductor [3]. The experimental realization of those remains elusive, expect for the QAH effect, which exhibits spin polarized, dissipationless, chiral edge-state transport in the absence of external magnetic fields and which has been observed in charge compensated, Cr and/or V doped TIs [4–6]. However, doped TIs suffer from several disadvantages including an inhomogeneous magnetic gap opening across the surface, partial magnetic volume fraction at low doping levels and the presence of impurity bands that can significantly limit their applicability [7–11]. Therefore, the proximity to an insulating magnetic layer was proposed as an alternative approach to breaking time reversal symmetry at the surface of a TI. As a consequence, interfaces between TIs and magnetic insulators have been investigated with a large number of different material combinations [12–22]. The hope is that such interfaces allow for more homogeneous properties across the surface and induce a magnetic gap via magnetic exchange coupling in the TSS that forms at the boundary between the TI and the topologically trivial magnetic insulator. Another advantage is that the magnetic transition temperature is

given by the choice of the magnetic layer and can be much higher than for magnetically doped TIs [14, 19, 21, 22]. A related promising strategy, proposes to use magnetic layers that are chemically similar to the TI and grown directly on its surface. This approach, called magnetic extension, has recently been explored with Bi<sub>2</sub>MnSe<sub>4</sub> based compounds [23–25].

One of the candidate insulating magnets that has a structure compatible with the Bi<sub>2</sub>Se<sub>3</sub> TI family is EuS. The EuS layer orders ferromagnetically in-plane with a Curie temperature  $T_C^{\text{EuS}} \approx 16$  K. It has been shown with polarized neutron reflectometry that at low temperature there is a large induced in-plane magnetic moments extending typically  $\sim 2$  nm into the TI [16, 18, 20]. Theoretically, such an in-plane magnetic anisotropy could be sufficient to realize the QAH effect if it breaks the reflection symmetry of the TI [26]. However, in EuS/Bi<sub>2</sub>Se<sub>3</sub> there is evidence for a tilting of the moments at the interface, generating an out-of-plane component which can induce a conventional exchange gap [12, 17]. But most surprisingly, it has been reported that a magnetic moment at the interface persists up to room temperature (RT), thereby largely exceeding  $T_C^{\text{EuS}}$ , which makes this interface potentially interesting for spintronics application [16].

The origin of these unusual properties, in particular the high magnetic transition temperature, were attributed to the presence of TSS at the EuS/TI interface [16, 20]. Indeed, the proximity induced in-plane moment measured in PNR in charge compensated (Bi,Sb)<sub>2</sub>Te<sub>3</sub>/EuS is maximal and decreases under the application of positive or

negative back-gate voltage [20]. This hints at the involvement of the TSS in the magnetic coupling, but could also be explained by different screening behaviors of TSS and bulk bands [20].

The absence of the QAH effect in current EuS/(charge compensated TI) devices may be due to a small overlap between the TSS and the localized Eu 4f states which would result in a small exchange interaction between the TI and EuS [27]. Moreover, the exchange coupling should be significant only on a length scale of a few Å and the formation of a topologically trivial interface state is expected [28]. Density functional theory (DFT) calculations on EuS/Bi<sub>2</sub>Se<sub>3</sub> confirm the formation of such a trivial interface state inside the bandgap of the TI and suggest that the topological state is almost gapless for thick Bi<sub>2</sub>Se<sub>3</sub> layers [29–31]. This is attributed to the fact that the TSS are shifted away from the interface and deeper into the TI [30]. Experimentally, the absence of EuS’s Raman peaks in the presence of a adjacent Bi<sub>2</sub>Se<sub>3</sub> layer points to the presence of significant band-bending in EuS [32]. Therefore, the nature of the magnetism at the EuS/Bi<sub>2</sub>Se<sub>3</sub> interface remains unclear and highly debated, in particular with regards to the interplay between topology and magnetism.

Here, we address this question directly using depth resolved measurements of the local magnetic and electronic properties of EuS/Bi<sub>2</sub>Se<sub>3</sub> heterostructures using muon spin spectroscopy ( $\mu$ SR) and soft X-ray angle resolved photoemission spectroscopy (SX-ARPES) at the buried interface. By tuning the photon energy ( $h\nu$ ) to the Eu anti-resonance at the Eu  $M_5$  pre-edge we find a clear photoemission signal of the Bi<sub>2</sub>Se<sub>3</sub> conduction band, through a protective Al<sub>2</sub>O<sub>3</sub> capping layer and the EuS layer. This allows us to confirm that the electronic structure of the buried Bi<sub>2</sub>Se<sub>3</sub> layer is preserved in the presence of the EuS and capping layer. Our  $\mu$ SR measurements show that below the magnetic transition of EuS, there are strong local magnetic fields which extend several nanometers into the adjacent TI layer and completely depolarize the muons. Comparison between the properties of the EuS/Bi<sub>2</sub>Se<sub>3</sub> and EuS/titanium interfaces reveals that they are very similar magnetically, implying that the presence of TSS at the interface are most probably not a dominant factor in the observed proximity effect at these interfaces.

## EXPERIMENT

The studied samples consist of layers of Bi<sub>2</sub>Se<sub>3</sub>, V<sub>0.2</sub>(Bi<sub>0.32</sub>Sb<sub>0.68</sub>)<sub>1.8</sub>Te<sub>3</sub> and Ti grown onto sapphire (0001) substrates by molecular beam epitaxy [33, 34]. A layer of EuS was added by evaporation using an electron-beam source at room temperature [16]. Finally, all samples were capped with an amorphous Al<sub>2</sub>O<sub>3</sub> layer to protect them during *ex-situ* transportation. The thickness

of both the Al<sub>2</sub>O<sub>3</sub> and EuS was 4 nm for the  $\mu$ SR experiments and 1 nm for ARPES. All samples and their corresponding layer compositions are listed in Table I. The thickness of the topological insulators is given in

Cap	EuS	Interlayer	Technique
4 nm Al <sub>2</sub> O <sub>3</sub>	4 nm	20 QL Bi <sub>2</sub> Se <sub>3</sub>	LE- $\mu$ SR
4 nm Al <sub>2</sub> O <sub>3</sub>	4 nm	20 QL V <sub>0.2</sub> (Bi <sub>0.32</sub> Sb <sub>0.68</sub> ) <sub>1.8</sub> Te <sub>3</sub>	LE- $\mu$ SR
4 nm Al <sub>2</sub> O <sub>3</sub>	4 nm	60 nm Ti	LE- $\mu$ SR
4 nm Al <sub>2</sub> O <sub>3</sub>	4 nm	60 QL Bi <sub>2</sub> Se <sub>3</sub>	LE- $\mu$ SR
1 nm Al <sub>2</sub> O <sub>3</sub>	1 nm	10 QL Bi <sub>2</sub> Se <sub>3</sub>	SX-ARPES
10 nm Se	-	10 QL Bi <sub>2</sub> Se <sub>3</sub>	SX-ARPES

TABLE I: Nominal thicknesses of the investigated samples, grown on sapphire (0001) substrates.

quintuple layers (1 QL  $\approx$  1 nm). The layer thickness and interface quality of the  $\mu$ SR samples has been verified by Rutherford backscattering (RBS) at the Tandem accelerator of ETH Zurich.

The SX-ARPES experiments were performed with p-polarized light on the ADDRESS beamline (X03MA) at the Swiss Light Source, Paul Scherrer Institut, Villigen, Switzerland [35]. During the measurements the temperature was kept below 12 K and the analyzer slit was oriented along the incident X-ray direction [36]. The combined beamline and analyzer resolution at  $h\nu = 1.12$  keV was better than 220 meV. The heterostructures were probed through the amorphous 1 nm Al<sub>2</sub>O<sub>3</sub> capping layer. The higher photoelectron escape depth of SX-ARPES in comparison to standard UV-ARPES allows to retrieve information from underneath such a thin layer [37]. In addition, we investigated reference samples of Bi<sub>2</sub>Se<sub>3</sub> protected by a Se capping layer, which was removed *in situ* before the measurement [38]. All samples were investigated with the same beamline and analyzer settings. Supporting X-ray absorption spectra (XAS) were recorded *in-situ* by detecting the total electron yield (TEY) via the drain current of the sample.

The low energy  $\mu$ SR experiments were performed on the  $\mu$ E4 beamline of the Swiss Muon Source at Paul Scherrer Institute in Villigen, Switzerland [39]. Fully spin-polarized muons were implanted into the sample with an implantation energy,  $E$ , tunable from 1 keV to 12 keV. The muons decay with a lifetime of  $\approx 2.2$   $\mu$ s into a positron and two neutrinos. Parity violation of this weak decay dictates that the decay positron is emitted preferentially along the muon spin direction [40]. Therefore, measuring the spatial distribution of the decay positrons with four detectors around the sample allows us to determine the ensemble average of the temporal evolution of the muon spin polarization. For these measurements the samples were glued on a Ni-coated sample plate, which suppresses the signal from muons missing the sample [41]. The measurements were performed in the temperature range of 4 K to 320 K and in a weak transverse field (wTF) of 5 mT, which was applied per-

pendicular to the sample surface. The data was analyzed with the `Musrfit` software [42]. The muon stopping distributions as a function of energy were modeled with the `Trim.SP` code [43].

## RESULTS

### Structural characterization using RBS

The thickness and stoichiometric properties of the layers were verified using RBS measurements. The RBS yield as a function of final He energy is shown in Fig. 1. The resulting layer thicknesses from these measurements are given in Table II. The listed values were used as

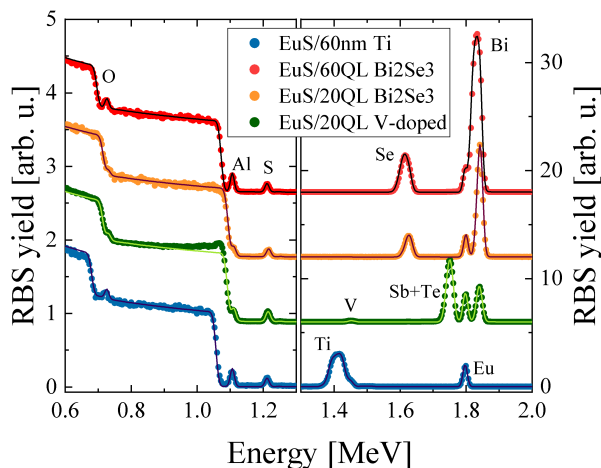


FIG. 1: RBS spectrum of 2 MeV He ions at a backscattering angle of  $168^\circ$ . The data is presented using a different offset and axis-scale in the left and right panel.

Interlayer	$\rho_{\text{Al}_2\text{O}_3}$	$\rho_{\text{EuS}}$	$\rho_{\text{Interlayer}}$
20 QL $\text{Bi}_2\text{Se}_3$	32.5	16.7	83.3
20 QL $\text{V}_{0.2}(\text{Bi}_{0.32}\text{Sb}_{0.68})_{1.8}\text{Te}_3$	47.5	22.8	74
60 QL $\text{Bi}_2\text{Se}_3$	55	15.1	178.9
60 nm Ti	55	15.2	-

TABLE II: Area number density of the layers determined by RBS in  $10^{15}$  at./ $\text{cm}^2$  of the samples investigated by LE- $\mu$ SR.

input parameter for all subsequent analysis. The composition of the various layers in the studied samples are confirmed to be free of impurities, except for the Ti layer which contains some additional transition metals (less than 20 at.% of mostly V and Co). In all samples, the EuS layer is found to be slightly S deficient, with the ratio Eu/S ranging from 0.85 to 0.96(3). The samples with 60 nm thick interlayers exhibit a sharp EuS/interlayer interface, whereas in the 20 nm samples the interlayer is extending slightly into the EuS layer. This could be due to

either interface roughness or intermixing, which cannot be distinguished by RBS.

### Electronic Properties using SX-ARPES

The ARPES intensity from a buried layer is usually very small. It is therefore helpful to first characterize a reference  $\text{Bi}_2\text{Se}_3$  sample independently before considering the full heterostructure. In Figure 2(a) we show the out-of-plane momentum  $k_z$  dependence (rendered from  $h\nu$ ) of the ARPES intensity of bare  $\text{Bi}_2\text{Se}_3$  at the Fermi level ( $E_F$ ) along the  $\Gamma$ -M direction. The observed Fermi intensity, composed of contributions from the conduction band and the TSS, exhibits periodic oscillations across the different  $\Gamma$  points in  $k_z$ , where the relative weight of the two components can vary [44]. A representative photoemission spectrum and a Fermi surface measured at  $h\nu = 1120$  eV are shown in Figs. 2(b,c) and Fig. 2(d), respectively.

For the heterostructure samples, which have been capped with an  $\text{Al}_2\text{O}_3$  layer of 1 nm thickness, we have confirmed the absence of any significant degradation by checking the Eu valence using XAS. The shape and position of the Eu  $M_5$  XAS peak in Fig. 3(c) clearly shows that Eu is mostly in the ferromagnetic  $\text{Eu}^{2+}$  state, cf. Ref. [45, 46]. However, we note that samples which were stored *ex-situ* (for several weeks) developed a considerable weight of  $\text{Eu}^{3+}$ . We suspect this is because of oxidation of the Eu through the thin capping layer.

Results of resonant photoemission spectroscopy measurements across the Eu  $M_{4,5}$  edges are shown in Fig. 3(a). In the vicinity of the Eu M edge, there is an enhanced cross section for coherent photoemission via intermediate  $3d^9 4f^{n+1}$  states, where  $n = 6$  or  $7$  for  $\text{Eu}^{3+}$  or  $\text{Eu}^{2+}$ , respectively. These second-order processes can interfere with direct photoemission, leading to a Fano-like lineshape of the intensity as a function of  $h\nu$  [47]. A comparison to the XAS spectrum reveals that the  $\text{Eu}^{2+}$  resonates around  $E_b \approx -1.7$  eV, whereas a small resonance of  $\text{Eu}^{3+}$  atoms is found at higher  $h\nu$  around  $E_b \approx -5$  eV. Figure 3(b) shows the integrated intensity of the  $\text{Eu}^{2+}$  PES peak across the Eu  $M_5$  and  $M_4$  edges. As expected, the resonant photoemission intensity follows a Fano-profile with a pronounced anti-resonance at the pre-edge. A similar anti-resonance behavior is often observed in resonant photoemission on transition metals [48–50].

Despite the large probing depth of SX-ARPES, observation of a weak dispersive signal from the buried  $\text{Bi}_2\text{Se}_3$  is hindered by overwhelming intensity around  $E_b \approx -1.7$  eV, which mainly corresponds to a  ${}^7\text{F}$  final state multiplett excited from  $\text{Eu}^{2+}$  [51, 52, Fig. 3(a)]. However, the Eu  $M_5$  anti-resonance at  $h\nu = 1120$  eV offers a favorable photon energy to “see through” the capping layers: The size of the Eu contribution around

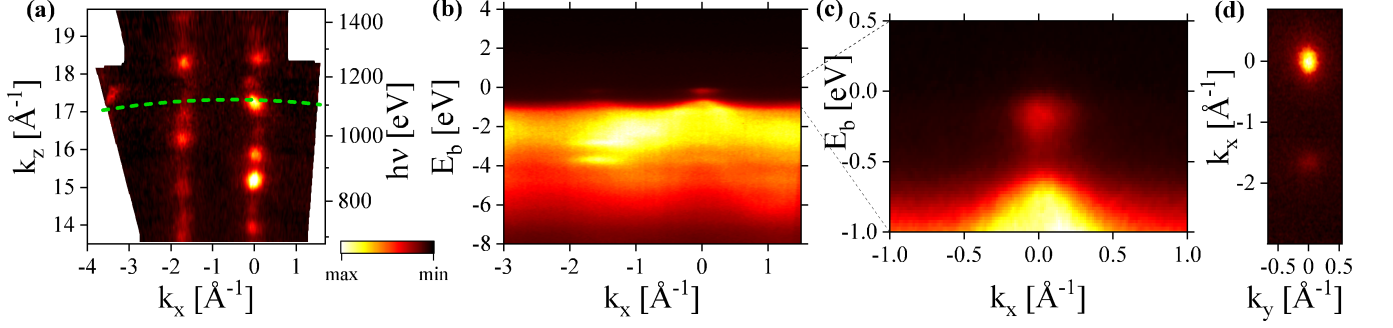


FIG. 2: (a) Fermi surface map of bare  $\text{Bi}_2\text{Se}_3$  along  $(k_x, k_z)$ . The corresponding  $h\nu$  values at  $k_x = 0$  are shown in the right axis. The dashed line indicates  $h\nu = 1120$  eV. (b),(c) High statistics cut at  $h\nu = 1120$  eV showing the conduction band and hints of the surface states of  $\text{Bi}_2\text{Se}_3$ . (d) Fermi surface cut around the  $\Gamma$  point at  $h\nu = 1120$  eV.

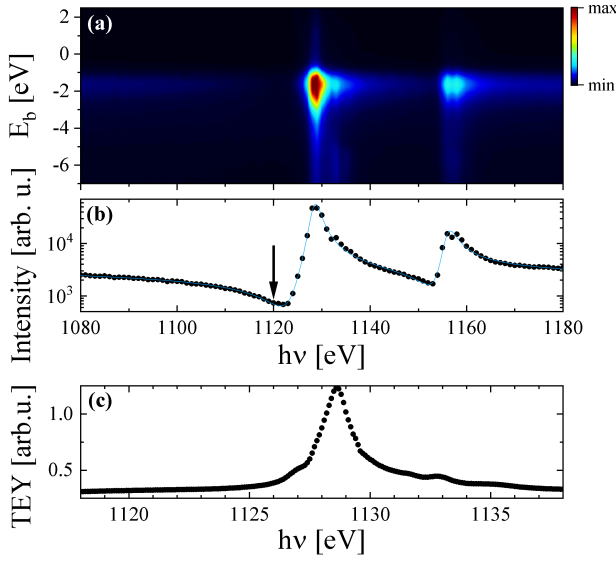


FIG. 3: (a) Angular integrated PES showing the resonating valence states at the Eu  $M_4$  and  $M_5$  edges. (b) Intensity of the resonating Eu peak (at  $E_b \approx -1.7$  eV). The solid line depicts a sum of two Fano profiles and a linear background. The arrow indicates  $h\nu = 1120$  eV. (c) XAS at the Eu  $M_5$  edge.

$E_b \approx -1.7$  eV is reduced by almost a factor of 4 [Fig. 3] and it lies close to a  $\Gamma$  point of bare  $\text{Bi}_2\text{Se}_3$  in  $k_z$ , where the conduction band and the surface states are expected to be seen [Fig. 2]. A high statistics measurement at this energy is shown in Fig. 4(a)-(c). It reveals dispersive spectral weight close to  $E_F$  at the  $\Gamma$  point. Since  $\text{Al}_2\text{O}_3$  is amorphous, the Eu 4f electrons in EuS are very localized and both layers are insulating, none of them should exhibit a dispersion close to  $E_F$ . Therefore, the observed dispersing features come from the buried  $\text{Bi}_2\text{Se}_3$  layer or its interface with EuS. To confirm this origin, we show a Fermi surface cut at the same  $h\nu$  in Fig. 4(d). It exhibits a hexagonal Brillouin zone pattern characteristic of  $\text{Bi}_2\text{Se}_3$ .

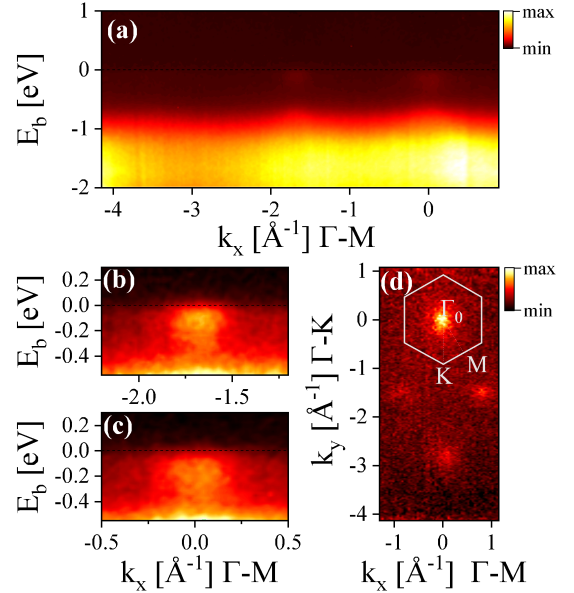


FIG. 4: (a) Band structure of the buried  $\text{Bi}_2\text{Se}_3$  at  $h\nu = 1120$  eV along  $\Gamma$ -M and seen through the caps of  $\text{Al}_2\text{O}_3$  and EuS. (b),(c) Zoom on the  $\Gamma_1$  and  $\Gamma_0$  points, respectively. (d) Fermi surface measured with the sample oriented along the  $\Gamma$ -K direction.

### Magnetic Properties using LE- $\mu$ SR

Representative  $\mu$ SR asymmetry spectra of EuS/(20 QL)  $\text{Bi}_2\text{Se}_3$  are shown in Fig. 5. The measured asymmetry exhibits a weakly damped oscillation at room temperature, as is typical for a paramagnetic sample [53]. With decreasing temperature, there is a slight reduction of the oscillation amplitude and at 5 K it becomes a much smaller and the oscillation is heavily damped. This indicates that the implanted muons experience a broad distribution of magnetic fields in a part of the sample, particularly in the EuS layer. There is an additional fast depolarization of a small part of the signal that is attributed to muons

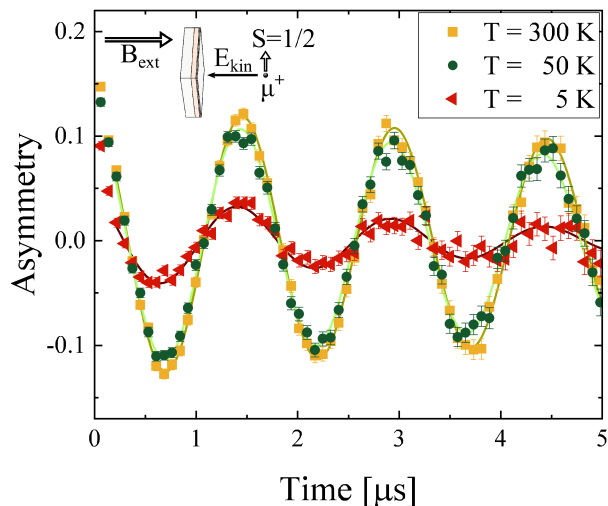


FIG. 5: Weak transverse field asymmetry spectra of 1.5 keV muons in the 4 nm Al<sub>2</sub>O<sub>3</sub>/4 nm EuS/20 QL Bi<sub>2</sub>Se<sub>3</sub> sample at different temperatures in an applied field of 5 mT. The inset depicts the measurement geometry.

stopping in the magnetic Ni coated sample holder and in the sapphire capping layer and substrate [41, 54]. These contributions have been subtracted by fitting the data measured after 0.2 μs to an exponentially damped cosine [11], see appendix for details.

The initial asymmetry,  $A_0$ , as a function of the implantation energy  $E$  for EuS/(60 QL) Bi<sub>2</sub>Se<sub>3</sub> and EuS/(60 nm)Ti is shown in Figs. 6(a) and 6(c), respectively [63]. We find that the behavior of  $A_0$  depends strongly on the implantation energy  $E$  and thereby on the probed layer, cf. Figs. 6(b) and 6(d). The signal is almost temperature independent at intermediate  $E$  ( $\sim 5 - 8$  keV), where most of the muons stop deep in the interlayer, whereas at low  $E$  ( $\lesssim 4$  keV), where most of the muons stop in the vicinity of the EuS/interlayer interface, there is a large drop in  $A_0$  as the temperature is decreased.

In Figure 7 we compare the temperature dependence of this drop for different samples. The data sets have been normalized to their RT values. An implantation energy of  $E = 1.5$  keV was used, in order to maximize the number of muons stopping close to the EuS/interlayer interface. All samples exhibit a gradual decrease in  $A_0$  with decreasing temperature and a sharp drop below  $T_C^{\text{EuS}} \sim 16$  K. Additional measurements in zero and longitudinal magnetic field (not shown) indicate that this drop is primarily due to static magnetism, causing an additional depolarization of the muon spin that can be almost fully decoupled upon application of 10 mT longitudinal field.

The V<sub>0.2</sub>(Bi,Sb)<sub>1.8</sub>Te<sub>3</sub> layer is expected to have a broad magnetic transition with an onset around  $T_C \approx 150$  K [11]. Indeed we observe two sequential drops of  $A_0$  in EuS/V<sub>0.2</sub>(Bi,Sb)<sub>1.8</sub>Te<sub>3</sub>: One below 150 K fol-

lowed by a second one at  $\sim 16$  K, corresponding to  $T_C^{\text{EuS}}$  [Fig. 7]. The first drop is accompanied by both a decrease of the mean field and an increase of the depolarization rate [Fig. 10] which is consistent with our previous measurements [11]. Both of these properties are mostly unaffected by the magnetic transition of the EuS layer. This is not very surprising, since the signal from the V-doped layer is lost already above  $T_C^{\text{EuS}}$ . However, this situation is different in the other samples, where the transition of EuS is accompanied by a decrease of the mean field in the sample and a peak in the depolarization rate [Figs. 10 and 11].

## DISCUSSION

### Electronic properties

In DFT calculations of EuS/Bi<sub>2</sub>Se<sub>3</sub>, a sharp interface between a Se and Eu layer is typically assumed. This leads to the presence of a topologically trivial interface state that crosses the Fermi surface between  $\Gamma$ -K and forms a plateau at the M point along  $\Gamma$ -M around  $E_b \approx -0.2$  eV [29–31]. Some calculations further predict an EuS derived band which dips below  $E_F$  at the M-point [31]. However, recent DFT results suggest that the presence of these trivial states depends on the assumed interface structure [55]. Indeed, we observe none of these bands experimentally. This may be due to a different arrangement of the atoms at the interface than what was originally assumed in DFT. But we cannot exclude the presence of interface roughness which could prevent the interface states from forming with a clear in-plane dispersion, or simply a very low photoemission cross section with the interface states at  $h\nu = 1120$  eV. Even in bare Bi<sub>2</sub>Se<sub>3</sub> the instrumental resolution is insufficient to resolve the dispersion of the TSS and distinguish it from the bulk conduction band, Fig. 2(c). Hence, it is possible that the spectrum mainly consists of the bulk conduction band that is smeared across the gap by the experimental resolution.

A detailed comparison of the momentum and energy distribution curves (MDC and EDC, respectively) of the EuS/Bi<sub>2</sub>Se<sub>3</sub> and bare Bi<sub>2</sub>Se<sub>3</sub> reveals a very similar dispersion [Fig. 8]. The MDCs around the  $\Gamma_0$  point and within the band gap of EuS are only slightly broader in EuS/Bi<sub>2</sub>Se<sub>3</sub> compared to Bi<sub>2</sub>Se<sub>3</sub>. In contrast, the EDCs at  $\Gamma_0$  are different in the two samples: We observe a plateau between  $E_F$  and  $-0.6$  eV in EuS/Bi<sub>2</sub>Se<sub>3</sub>, whereas in bare Bi<sub>2</sub>Se<sub>3</sub> there is a clear dip around  $-0.45$  eV. However, in EuS/Bi<sub>2</sub>Se<sub>3</sub> a significant part of the spectral weight is non-dispersive. In order to compare only the dispersive part to bare Bi<sub>2</sub>Se<sub>3</sub> we consider the difference between the EDCs at  $\Gamma$  and M, where we don't see any dispersion. This is shown as a yellow line in Fig. 8(b), revealing a qualitatively similar behavior to bare Bi<sub>2</sub>Se<sub>3</sub>.

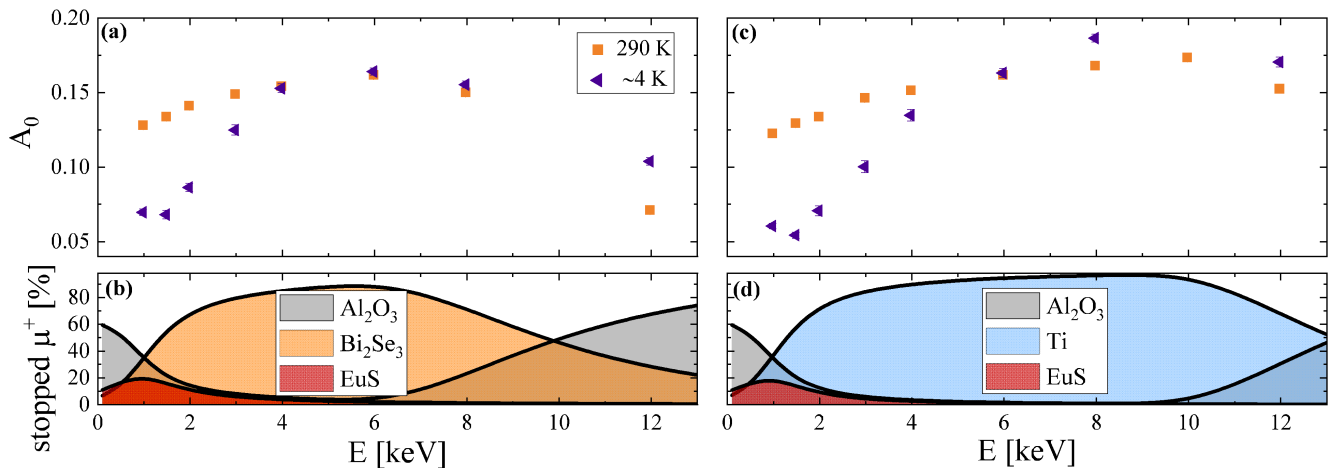


FIG. 6: Initial asymmetry  $A_0$  as a function of implantation energy  $E$  in the (a) EuS/(60 QL) Bi<sub>2</sub>Se<sub>3</sub> and (c) EuS/(60 nm)Ti samples. (b) and (d) show the corresponding calculated stopping fractions.

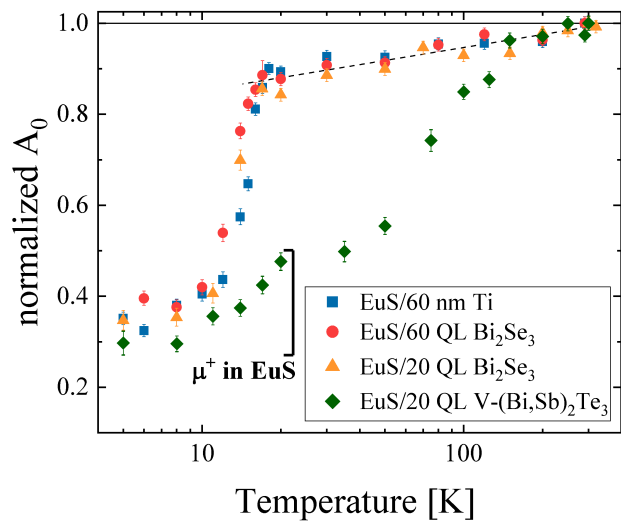


FIG. 7: Initial asymmetry at 1.5 keV implantation energy normalized to the RT value as a function of temperature. The black bar indicates the fraction of muons stopping in the EuS layer of the V-doped sample. The black lines are guides to the eye.

This indicates that the dispersive line shape of the buried Bi<sub>2</sub>Se<sub>3</sub> remains mostly unaffected by the presence of EuS.

Nevertheless, we note a clear discrepancy between EuS/Bi<sub>2</sub>Se<sub>3</sub> and bare Bi<sub>2</sub>Se<sub>3</sub> in the relative intensity of the conduction band at the  $\Gamma_0$  and  $\Gamma_1$  points. While the intensity at  $\Gamma_1$  is much lower than at  $\Gamma_0$  in bare Bi<sub>2</sub>Se<sub>3</sub>, the two points have a comparable spectral weight in EuS/Bi<sub>2</sub>Se<sub>3</sub> [Figs. 2(b) and 4(a)]. To exclude that this is an artifact of misalignment an MDC that was additionally integrated within  $k_y = \pm 0.15 \text{ \AA}^{-1}$  around the  $\Gamma$  point [64] is shown in Fig. 8(c). The large difference between the two curves implies that the matrix element of the photoemission process is altered in presence of the

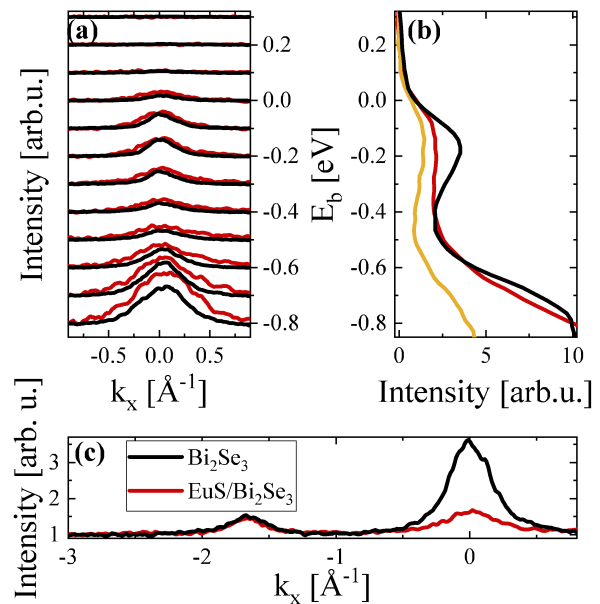


FIG. 8: (a) MDCs of EuS/(10 QL) Bi<sub>2</sub>Se<sub>3</sub> in comparison to MDCs of bare Bi<sub>2</sub>Se<sub>3</sub>. (b) EDC at the  $\Gamma$  point integrated within  $k_x = \pm 0.1 \text{ \AA}^{-1}$ . In order to reduce the contribution from non-dispersive spectral weight in EuS/(10 QL) Bi<sub>2</sub>Se<sub>3</sub>, the yellow line shows the difference between the EDC around  $\Gamma$  and around M. (c) Total intensity within  $-0.3 \text{ eV}$  below  $E_F$  and within  $k_y = \pm 0.15 \text{ \AA}^{-1}$  around  $\Gamma$ . The scale between measured intensities on EuS/(10 QL) Bi<sub>2</sub>Se<sub>3</sub> and bare Bi<sub>2</sub>Se<sub>3</sub> is arbitrary and different in each subplot.

EuS layer. The origin of this large change can be qualitatively understood by approximating the matrix element with the weights of the Fourier decomposition of the initial state wavefunction [56, 57].  $\Gamma_0$  and  $\Gamma_1$  correspond to the zeroth and first order in-plane Fourier coefficients, but the high  $h\nu$  selects a higher order out-of-plane component from them. It seems plausible that such weights

of the higher harmonics in  $k_z$  (i.e. sharp details of the wavefunction) may change in the presence of the EuS interface without causing a considerable change to the spectral lineshapes. Therefore, we find clear evidence of a modification of the initial state wave function caused by the presence of the top layers.

### Local magnetic properties

Zero-field measurements in the magnetic phase of bulk samples of EuS have shown that the local field at the muon stopping position is on the order of 0.336 T [58]. In the weak transverse field measurements that we report here, such strong magnetic fields will cause the observed loss of  $A_0$ . Therefore, our results are consistent with previous measurements that reported ferromagnetic ordering in the EuS thin layer [12, 16, 17].

The energy and temperature dependence of  $A_0$  in Fig. 6 can be qualitatively understood, by comparing it to the simulated stopping fractions: At high implantation energies, the behavior can be fully explained by the temperature dependence of muons in sapphire, which show an increase of  $A_0$  towards low temperature [11, 59]. The pronounced loss of  $A_0$  at low temperature and low implantation energy is attributed to the magnetism in the EuS layer and at its interface. The temperature independent full asymmetry at intermediate energies, where most muons stop deep in the  $\text{Bi}_2\text{Se}_3$  or Ti layer, is a clear signature that any interface effects vanish further inside the material.

We now turn to a quantitative estimation of the magnetic volume fraction in the samples. From the calculated muon stopping profile of  $\text{EuS}/\text{V}_{0.2}(\text{Bi,Sb})_{1.8}\text{Te}_3$  we expect that  $\sim 23\%$  of the muons stop in the EuS layer when using an implantation energy of 1.5 keV. The measured asymmetry is an ensemble average over all muons in the sample. Therefore, if we assume that only muons stopping in the EuS layer are depolarized, we expect to observe a 23% decrease relative to the full asymmetry in this sample as indicated with a bar in Fig. 7. This is consistent with our observation, since all muons stopping in the magnetic TI layer are already fully depolarized above  $T_C^{\text{EuS}} \sim 16$  K. In the other samples, the EuS layer is slightly thinner [Table II] and following the same logic we expect a smaller drop of about 15% in the asymmetry. However, we observe a much larger drop instead. This is a clear indication that large magnetic fields extend to regions outside the EuS layer, in particular into the interlayer beneath. The large drop in  $A_0$  can only be accounted for if muons stopping several nm inside the  $\text{Bi}_2\text{Se}_3$  and Ti layer are also depolarized.

The fact that the size of the drop at  $T_C^{\text{EuS}}$  in  $\text{EuS}/\text{V}_{0.2}(\text{Bi,Sb})_{1.8}\text{Te}_3$  is correctly predicted by the simulation, further attests to the accuracy of the `Trim.SP` results and justifies their use to make rough estimation

of the involved length scale of the region influenced by the magnetic layer in the other samples. In these estimates we use the calculated muon stopping profiles shown in Figs. 9(a) and 9(c). In order to evaluate the measured asymmetry, we assume that muons stopping in EuS do not contribute, while those stopping in the sapphire substrate contribute only 42% of their polarization [11]. In addition, muons stopping in the interlayer are assumed to contribute fully to the polarization. The result of this calculation is shown as a black line in Figs. 9(b) and 9(d). Here, the total  $A_0$  was scaled to match the point measured at RT and  $E = 6$  keV, where most muons stop in the interlayer. As expected, this curve overestimates  $A_0$  at low implantation energy and recovers to the RT values too quickly with increasing energy. To better account for our measurements, we introduce an additional ‘‘proximity magnetized’’ layer of thickness  $d$  in the near-interface region of the interlayer, close to EuS. We assume that muons stopping in this layer are also depolarized rapidly and do not contribute to the measured asymmetry. The calculated curves for various values of  $d$  are shown in Fig. 9. They mimic more closely our measurements for  $d = 4 - 8$  nm, though not perfectly. The discrepancy can, at least partially, be attributed to our simplistic assumption of a uniform, step-like magnetization profile, which is most probably not the case in these samples. Other possible sources of deviation include uncertainties in the number of backscattered muons and effects of the magnetism in EuS onto the  $\text{Al}_2\text{O}_3$  capping. However, the results on  $\text{EuS}/\text{V}_{0.2}(\text{Bi,Sb})_{1.8}\text{Te}_3$  in Fig. 7 indicate that the effect of the latter is very small.

We conclude that our calculations provide a rough estimate of the thickness of the affected region, between 4 – 8 nm for *both*  $\text{EuS}/(60 \text{ QL}) \text{Bi}_2\text{Se}_3$  and  $\text{EuS}/(60 \text{ nm})\text{Ti}$ , which is larger than the 2 nm proximity that is typically observed with PNR [16, 18, 20]. This discrepancy is primarily due to the higher sensitivity of  $\mu\text{SR}$  to small magnetic fields compared to PNR. Moreover, while an effective depolarization of the muon spin can be caused by a strong field in an arbitrary direction, the PNR experiments are sensitive only to the in-plane component of the magnetization. For example, in the  $\text{EuS}/\text{V}_{0.2}(\text{Bi,Sb})_{1.8}\text{Te}_3$  the local magnetic fields are strong enough to completely depolarize the muons, while the corresponding magnetic scattering length density in PNR is very small [11, 18]. As discussed in the Appendix, the small negative shift of the field below  $T_C^{\text{EuS}}$  could be consistent with previously reported out-of-plane components of the magnetism at the interface, generating long range stray fields that would not have been seen with PNR [12, 17].

Note that the depolarization of the muons within 4 – 8 nm adjacent to the interface could be caused either by proximity induced magnetism or by stray fields, e.g. due to roughness of the interface or finite magnetic domain size in the EuS layer. However, while the prox-

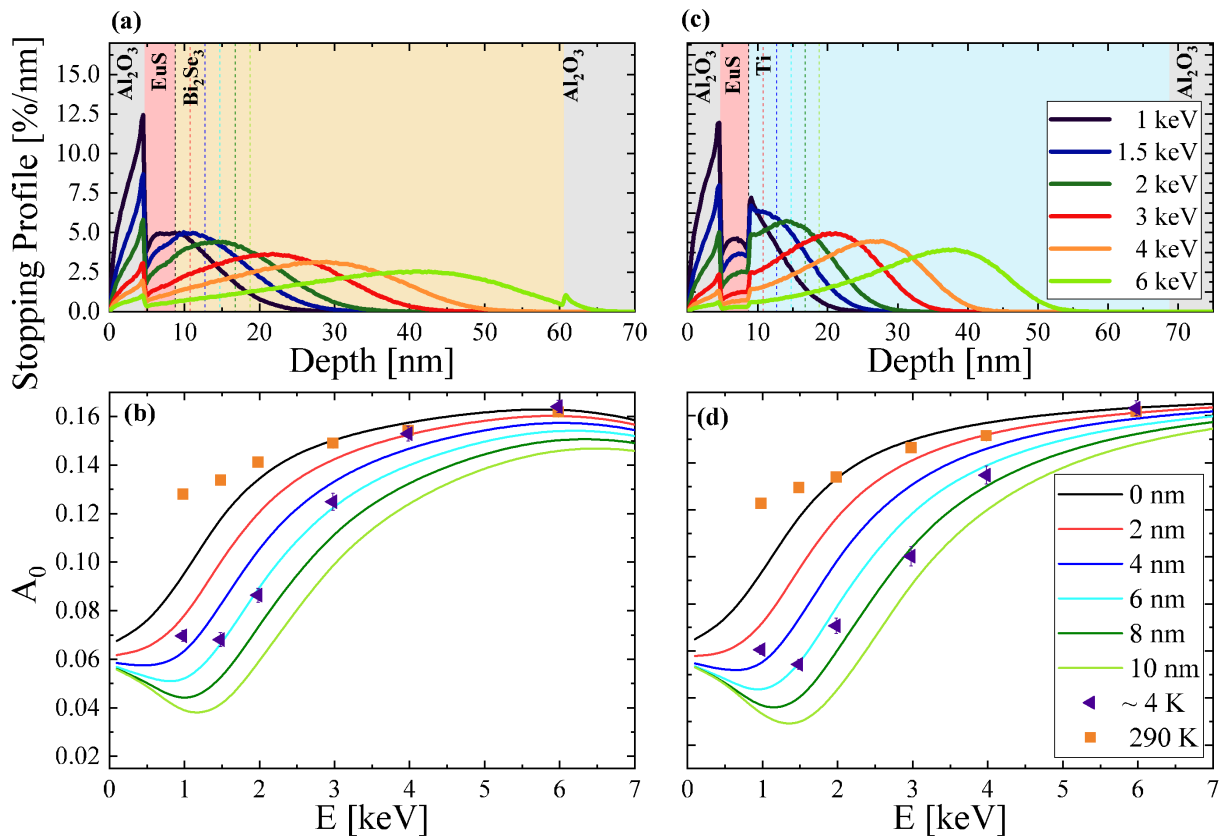


FIG. 9: Muon implantation profiles for different implantation energies in the (a) 60 QL  $\text{Bi}_2\text{Se}_3$  and (c) Ti samples. (b) and (d) show the corresponding initial asymmetries  $A_0$  as a function of implantation energy  $E$  (i.e. a zoom into Fig. 6(a) and 6(c)). The solid lines show the calculated asymmetry where the muons stopping within the first  $n$  nm of the interlayer are completely depolarized. The depths of the magnetic proximity corresponds to the dashed lines of the same color in (a) and (c).

imity effect, mediated by the TSS or bulk metallic states, should occur close to the interface (within a few Å, [28]), the relevant depth scale for stray fields is given by the length scale of the domains/modulation due to roughness [60]. In our samples the roughness is expected to be much smaller than 4 nm and should be a minor contribution [12, 16]. Therefore, the observed depolarization several nanometers inside the interlayer is most likely dominated by stray fields originating from magnetic domains.

Surprisingly, there is a slow and gradual decrease of  $A_0$  with decreasing temperature in all samples already above the EuS transition (indicated with a dashed line in Fig. 7). Such a decrease is typically absent in non-magnetic samples and other undoped TI thin films [11]. For example, calibration measurements on a gold film show a temperature independent initial asymmetry, thus excluding experimental artifacts. Instead, this effect could be a sign of interface magnetism persisting up to room temperature, in agreement with Ref. [16]. Note that Ti has very small nuclear moments which are expected to produce only a very slow damping of the  $\mu\text{SR}$  asymmetry [61, 62]. It should thus be the ideal reference sample as a topologically trivial metal. Therefore,

the decrease of the asymmetry with decreasing temperature, cannot be caused by the presence of topological interface states. There are two possible scenarios that could explain the observed decrease: First, it has an origin unrelated to interface magnetism. In this case, our results imply that there is no significant enhancement of the transition temperature in our samples of EuS/ $\text{Bi}_2\text{Se}_3$ . Second, the decrease is caused by a magnetic interface effect (within  $\sim 1$  nm of the interface) that persists up to RT. However this would imply that the same effect is present in EuS/(60 nm)Ti.

Another unexpected feature in Fig. 7, is that even below  $T_C^{\text{EuS}}$ , the curves measured in both samples (EuS/(60 QL)  $\text{Bi}_2\text{Se}_3$  and EuS/(60 nm)Ti) are identical within our experimental accuracy. This is a strong indication that the magnetic fields extending into the interlayer are very similar, but most importantly, they seem to be unaffected by the topology of the metallic states at the interface. Since the size of this effect is the same in both materials, we conclude that this property is intrinsic to the EuS/metal interface.



## CONCLUSION

We combine several depth sensitive experimental techniques to investigate the magnetic proximity effect in EuS/Bi<sub>2</sub>Se<sub>3</sub>. Our  $\mu$ SR measurements reveal the presence of large local magnetic fields that extend several nanometers away from the EuS layer and into the adjacent non-magnetic layer. However, this length scale indicates that the main contribution to the detected fields in the non-magnetic layer is stray fields from EuS magnetic domains. A careful comparison between EuS/Bi<sub>2</sub>Se<sub>3</sub> and EuS/Ti reveals a qualitatively similar behavior which implies that it does not rely upon the presence of topological states at the interface. Rather, the dominant contribution to the observed local magnetic properties appears to be independent of the topology and the exact electronic structure at the interface. Using anti-resonant SX-ARPES at the Eu M<sub>5</sub> pre-edge we find that the dispersive electronic band structure of the buried Bi<sub>2</sub>Se<sub>3</sub> layer remains mostly unaffected by the presence of the EuS and Al<sub>2</sub>O<sub>3</sub> layers. There is no clear signature of the previously predicted interface states [29–31], hinting at a different interface structure. However, we find a change of the relative spectral weight across different Brillouin zones, associated with an electronic reconstruction caused by the presence of EuS.

The combined LE- $\mu$ SR and SX-ARPES results show that there can be strong magnetic fields in the layer beneath EuS, unrelated to topological interface states or the presence of strong magnetic exchange coupling. However, both of those are desirable when considering topological insulator/magnetic insulator interfaces for QAH devices. Finally, to answer our initial question, the presented results can be fully explained without a need to introduce an interplay between topology and ferromagnetism at the EuS/Bi<sub>2</sub>Se<sub>3</sub> interface.

## Acknowledgments

This work is based on experiments performed at the Swiss Muon Source (S $\mu$ S) and Swiss Light Source (SLS), Paul Scherrer Institute, Villigen, Switzerland. The authors thank B. P. Tobler for his participation at the ARPES beamtime. The work at PSI was supported by the Swiss National Science Foundation (SNF-Grant No. 200021\_165910). C.-Z.C. Y.-B.O and J.S.M. acknowledge the support from NSF grant no. DMR-1700137, Office of Naval Research (ONR) grant no. N00014-16-1-2657, and the Science and Technology Center for Integrated Quantum Materials under NSF grant no. DMR-1231319. C.Z.C. thanks the support from Alfred P. Sloan Research Fellowship and ARO Young Investigator Program Award (W911NF1810198).

## Appendix: Detailed discussion of local fields measured with LE- $\mu$ SR

The  $\mu$ SR spectra were fitted to an exponentially damped cosine of the form

$$A(t) = A_0 e^{-\lambda t} \cos(\gamma_\mu B t + \varphi). \quad (1)$$

In the main text we mainly discuss the initial asymmetry at  $t = 0 \mu\text{s}$ ,  $A_0$ . However, the damping rate  $\lambda$  and the oscillation frequency  $\omega = \gamma_\mu B$  are also affected by the magnetic transition. Here,  $B$  is the mean magnetic field at the muons' stopping sites and  $\gamma_\mu = 2\pi \times 135.5 \text{ MHz/T}$  is the muon gyromagnetic ratio. Note that  $B$  is mostly sensitive to out-of-plane component of the internal magnetic field [65]. The initial phase  $\varphi$  reflects the initial orientation of the implanted muons and depends also on the geometrical details of the spectrometer. The temperature dependence of  $B$ ,  $\lambda$  and  $A_0$  is shown in Fig. 10 for the different topological insulator samples and in Fig. 11 for different implantation energies in EuS/(60 nm)Ti.

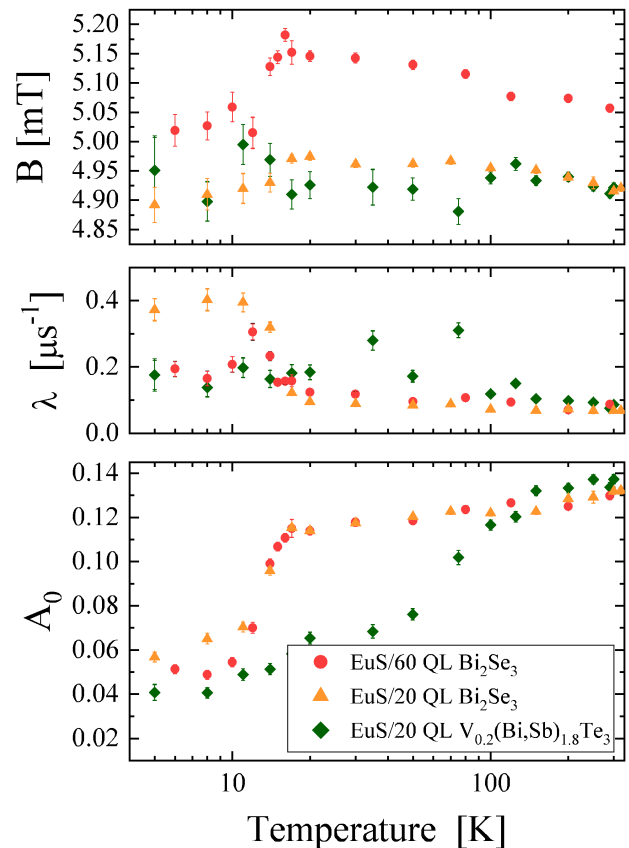


FIG. 10: Mean field, damping rate and initial asymmetry in wTF as a function of temperature for different TI samples, measured with an implantation energy of 1.5 keV.

The damping rate  $\lambda$  exhibits a peak at  $T_C^{\text{EuS}}$  in some samples and remains larger than the RT value at low temperature. This indicates an increase of the width of the

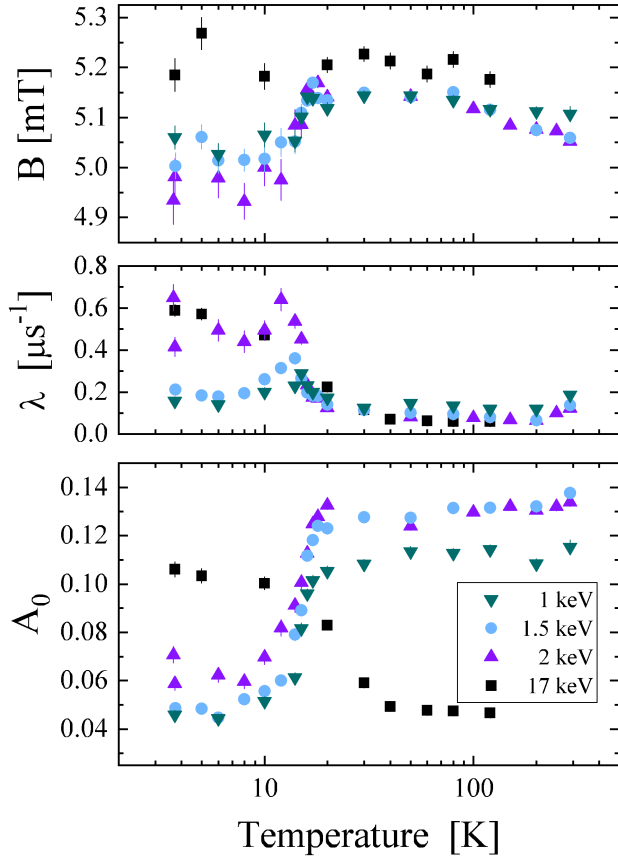


FIG. 11: Mean field, damping rate and initial asymmetry in wTF as a function of temperature in the EuS/(60 nm)Ti sample at different implantation energies. The points at 17 keV show the temperature dependence of the sapphire substrate.

static field distribution as well as some dynamic contributions at  $T_C^{\text{EuS}}$  due to critical fluctuations. The mean field  $B$  decreases at  $T_C^{\text{EuS}}$ , except in EuS/V<sub>0.2</sub>(Bi,Sb)<sub>1.8</sub>Te<sub>3</sub>. The fact that there is no shift at low temperature in that sample [Fig. 10] and no shift in EuS/(60 nm)Ti at high implantation energies, implies that the shift is unlikely to be caused by a background contribution. Instead, it originates inside the samples, in particular from somewhere with no long range magnetic order, but still close to the interface region. There are two interactions that may account for such a shift: stray fields and hyperfine coupling to polarized electrons that are screening the muon [53]. The latter would require that a polarization of the conduction electrons is induced several nm away from the interface. Moreover, the polarization would have to be out of plane unless the hyperfine coupling tensor had very large off-diagonal terms. Therefore, it is more likely that stray fields are the source of the observed field shift. Note that in-plane dipolar fields will exhibit a symmetric field distribution of out-of-plane fields. This implies that a purely in-plane inhomogeneity does not affect the out-of-plane mean field. The observed shift of  $B$  thus points

to the presence of out-of-plane stray fields close to the interface in both EuS/Bi<sub>2</sub>Se<sub>3</sub> and EuS/(60 nm)Ti.

\* Electronic address: [jonas.krieger@psi.ch](mailto:jonas.krieger@psi.ch)

† Electronic address: [vladimir.strocov@psi.ch](mailto:vladimir.strocov@psi.ch)

‡ Electronic address: [zاهر.salman@psi.ch](mailto:zاهر.salman@psi.ch)

- [1] R. Yu, W. Zhang, H.-J. Zhang, S.-C. Zhang, X. Dai, and Z. Fang, *Science* **329**, 61 (2010).
- [2] X.-L. Qi, T. L. Hughes, and S.-C. Zhang, *Physical Review B* **78**, 195424 (2008).
- [3] X.-L. Qi, T. L. Hughes, and S.-C. Zhang, *Physical Review B* **82**, 184516 (2010).
- [4] C.-Z. Chang, J. Zhang, X. Feng, J. Shen, Z. Zhang, M. Guo, et al., *Science* **340**, 167 (2013).
- [5] C.-Z. Chang, W. Zhao, D. Y. Kim, H. Zhang, B. A. Assaf, D. Heiman, S.-C. Zhang, C. Liu, M. H. W. Chan, and J. S. Moodera, *Nature Materials* **14**, 473 (2015).
- [6] Ou Yunbo, Liu Chang, Jiang Gaoyuan, Feng Yang, Zhao Dongyang, Wu Weixiong, Wang Xiao-Xiao, Li Wei, Song Canli, Wang Li-Li, et al., *Advanced Materials* **30**, 1703062 (2017).
- [7] I. Lee, C. K. Kim, J. Lee, S. J. L. Billinge, R. Zhong, J. A. Schneeloch, T. Liu, T. Valla, J. M. Tranquada, G. Gu, et al., *Proceedings of the National Academy of Sciences* **112**, 1316 (2015).
- [8] S. Grauer, S. Schreyeck, M. Winnerlein, K. Brunner, C. Gould, and L. W. Molenkamp, *Physical Review B* **92**, 201304 (2015).
- [9] E. O. Lachman, A. F. Young, A. Richardella, J. Cuppens, H. R. Naren, Y. Anahory, A. Y. Meltzer, A. Kandala, S. Kempinger, Y. Myasoedov, et al., *Science Advances* **1**, e1500740 (2015).
- [10] P. Sessi, R. R. Biswas, T. Bathon, O. Storz, S. Wilfert, A. Barla, K. A. Kokh, O. E. Tereshchenko, K. Fauth, M. Bode, et al., *Nature Communications* **7**, 12027 (2016).
- [11] J. A. Krieger, C.-Z. Chang, M.-A. Husanu, D. Sostina, A. Ernst, M. Otrokov, T. Prokscha, T. Schmitt, A. Suter, M. Vergniory, et al., *Physical Review B* **96**, 184402 (2017).
- [12] P. Wei, F. Katmis, B. A. Assaf, H. Steinberg, P. Jarillo-Herrero, D. Heiman, and J. S. Moodera, *Physical Review Letters* **110**, 186807 (2013).
- [13] Q. I. Yang, M. Dolev, L. Zhang, J. Zhao, A. D. Fried, E. Schemm, M. Liu, A. Palevski, A. F. Marshall, S. H. Risbud, et al., *Physical Review B* **88**, 081407 (2013).
- [14] M. Lang, M. Montazeri, M. C. Onbasli, X. Kou, Y. Fan, P. Upadhyaya, K. Yao, F. Liu, Y. Jiang, W. Jiang, et al., *Nano Letters* **14**, 3459 (2014).
- [15] B. A. Assaf, F. Katmis, P. Wei, C.-Z. Chang, B. Satpati, J. S. Moodera, and D. Heiman, *Physical Review B* **91**, 195310 (2015).
- [16] F. Katmis, V. Lauter, F. S. Nogueira, B. A. Assaf, M. E. Jamer, P. Wei, et al., *Nature* **533**, 513 (2016).
- [17] C. Lee, F. Katmis, P. Jarillo-Herrero, J. S. Moodera, and N. Gedik, *Nature Communications* **7**, 12014 (2016).
- [18] M. Li, C.-Z. Chang, B. J. Kirby, M. E. Jamer, W. Cui, L. Wu, P. Wei, Y. Zhu, D. Heiman, J. Li, et al., *Physical Review Letters* **115**, 087201 (2015).
- [19] S.-Y. Huang, C.-W. Chong, Y. Tung, T.-C. Chen, K.-C. Wu, M.-K. Lee, J.-C.-A. Huang, Z. Li, and H. Qiu,

- Scientific Reports **7**, 2422 (2017).
- [20] M. Li, Q. Song, W. Zhao, J. A. Garlow, T.-H. Liu, L. Wu, Y. Zhu, J. S. Moodera, M. H. W. Chan, G. Chen, et al., Physical Review B **96**, 201301 (2017).
- [21] Q. L. He, X. Kou, A. J. Grutter, G. Yin, L. Pan, X. Che, Y. Liu, T. Nie, B. Zhang, S. M. Disseler, et al., Nature Materials **16**, 94 (2017).
- [22] C. Tang, C.-Z. Chang, G. Zhao, Y. Liu, Z. Jiang, C.-X. Liu, M. R. McCartney, D. J. Smith, T. Chen, J. S. Moodera, et al., Science Advances **3**, e1700307 (2017).
- [23] T. Hirahara, S. V. Eremeev, T. Shirasawa, Y. Okuyama, T. Kubo, R. Nakanishi, R. Akiyama, A. Takayama, T. Hajiri, S.-i. Ideta, et al., Nano Letters **17**, 3493 (2017).
- [24] M. M. Otrokov, T. V. Meshchikova, I. P. Rusinov, M. G. Vergniory, V. M. Kuznetsov, and E. V. Chulkov, JETP Letters **105**, 297 (2017).
- [25] M. M. Otrokov, T. V. Meshchikova, M. G. Vergniory, I. P. Rusinov, A. Y. Vyazovskaya, Y. M. Koroteev, G. Bihlmayer, A. Ernst, P. M. Echenique, A. Arnau, et al., 2D Materials **4**, 025082 (2017).
- [26] X. Liu, H.-C. Hsu, and C.-X. Liu, Physical Review Letters **111**, 086802 (2013).
- [27] W. Luo and X.-L. Qi, Physical Review B **87**, 085431 (2013).
- [28] V. N. Men'shov, V. V. Tugushev, S. V. Eremeev, P. M. Echenique, and E. V. Chulkov, Physical Review B **88**, 224401 (2013).
- [29] A. T. Lee, M. J. Han, and K. Park, Physical Review B **90**, 155103 (2014).
- [30] S. V. Eremeev, V. N. Men'shov, V. V. Tugushev, and E. V. Chulkov, Journal of Magnetism and Magnetic Materials **383**, 30 (2015).
- [31] J. Kim, K.-W. Kim, H. Wang, J. Sinova, and R. Wu, Physical Review Letters **119**, 027201 (2017).
- [32] G. B. Osterhoudt, R. Carelli, K. S. Burch, F. Katmis, N. Gedik, and J. S. Moodera, Physical Review B **98**, 014308 (2018).
- [33] J. Zhang, C.-Z. Chang, Z. Zhang, J. Wen, X. Feng, K. Li, M. Liu, K. He, L. Wang, X. Chen, et al., Nature Communications **2**, 574 (2011).
- [34] C.-Z. Chang, J. Zhang, M. Liu, Z. Zhang, X. Feng, K. Li, L.-L. Wang, X. Chen, X. Dai, Z. Fang, et al., Advanced Materials **25**, 1065 (2013).
- [35] V. N. Strocov, T. Schmitt, U. Flechsig, T. Schmidt, A. Imhof, Q. Chen, J. Raabe, R. Betemps, D. Zimoch, J. Krempasky, et al., Journal of Synchrotron Radiation **17**, 631 (2010).
- [36] V. N. Strocov, X. Wang, M. Shi, M. Kobayashi, J. Krempasky, C. Hess, T. Schmitt, and L. Patthey, Journal of Synchrotron Radiation **21**, 32 (2014).
- [37] M. Kobayashi, I. Muneta, T. Schmitt, L. Patthey, S. Ohya, M. Tanaka, M. Oshima, and V. N. Strocov, Applied Physics Letters **101**, 242103 (2012).
- [38] K. Hofer, C. Becker, S. Wirth, and L. H. Tjeng, AIP Advances **5**, 097139 (2015).
- [39] T. Prokscha, E. Morenzoni, K. Deiters, F. Foroughi, D. George, R. Kobler, A. Suter, and V. Vrankovic, Nuclear Instruments and Methods in Physics Research Section A: Accelerators, Spectrometers, Detectors and Associated Equipment **595**, 317 (2008).
- [40] R. L. Garwin, L. M. Lederman, and M. Weinrich, Phys. Rev. **105**, 1415 (1957).
- [41] H. Saadaoui, Z. Salman, T. Prokscha, A. Suter, B. M. Wojek, and E. Morenzoni, Physics Procedia **30**, 164 (2012).
- [42] A. Suter and B. M. Wojek, Physics Procedia **30**, 69 (2012).
- [43] E. Morenzoni, H. Glückler, T. Prokscha, R. Khasanov, H. Luetkens, M. Birke, E. M. Forgan, C. Niedermayer, and M. Pleines, Nuclear Instruments and Methods in Physics Research Section B: Beam Interactions with Materials and Atoms **192**, 254 (2002).
- [44] R. Queiroz, G. Landolt, S. Muff, B. Slomski, T. Schmitt, V. N. Strocov, J. Mi, B. B. Iversen, P. Hofmann, J. Osterwalder, et al., Physical Review B **93**, 165409 (2016).
- [45] B. T. Thole, G. van der Laan, J. C. Fuggle, G. A. Sawatzky, R. C. Karnatak, and J.-M. Esteve, Physical Review B **32**, 5107 (1985).
- [46] L. L. Lev, D. V. Averyanov, A. M. Tokmachev, F. Bisti, V. A. Rogalev, V. N. Strocov, and V. G. Storchak, **5**, 192 (2016).
- [47] U. Fano, Physical Review **124**, 1866 (1961).
- [48] S. W. Robey, L. T. Hudson, and R. L. Kurtz, Physical Review B **46**, 11697 (1992).
- [49] Z. M. Stadnik, G. W. Zhang, A.-P. Tsai, and A. Inoue, Journal of Physics: Condensed Matter **6**, 6885 (1994).
- [50] M. Weinelt, A. Nilsson, M. Magnuson, T. Wiell, N. Wassdahl, O. Karis, A. Föhlisch, N. Mårtensson, J. Stöhr, and M. Samant, Physical Review Letters **78**, 967 (1997).
- [51] G. van der Laan and B. T. Thole, Physical Review B **48**, 210 (1993).
- [52] K. Yamamoto, K. Horiba, M. Taguchi, M. Matsunami, N. Kamakura, A. Chainani, Y. Takata, K. Mimura, M. Shiga, H. Wada, et al., Physical Review B **72**, 161101 (2005).
- [53] A. Yaouanc and P. de R'etotier, *Muon Spin Rotation, Relaxation, and Resonance: Applications to Condensed Matter*, International Series of Monographs on Physics (OUP Oxford, 2011).
- [54] J. D. Brewer, J. H. Brewer, G. D. Morris, D. G. Eshchenko, and V. G. Storchak, Physica B: Condensed Matter **289–290**, 428 (2000).
- [55] S. V. Eremeev, M. M. Otrokov, and E. V. Chulkov, Nano Letters **18**, 6521 (2018).
- [56] S. Moser, Journal of Electron Spectroscopy and Related Phenomena **214**, 29 (2017).
- [57] V. N. Strocov, Journal of Electron Spectroscopy and Related Phenomena **229**, 100 (2018).
- [58] D. G. Eshchenko, V. G. Storchak, E. Morenzoni, and D. Andreica, Physica B: Condensed Matter **404**, 903 (2009).
- [59] T. Prokscha, E. Morenzoni, D. G. Eshchenko, N. Garifianov, H. Glückler, R. Khasanov, H. Luetkens, and A. Suter, Physical Review Letters **98**, 227401 (2007).
- [60] E. Tsymbal, Journal of Magnetism and Magnetic Materials **130**, L6 (1994).
- [61] W. J. Kossler, H. E. Schone, K. Petzinger, B. Hitti, J. R. Kempton, E. F. W. Seymour, C. E. Stronach, W. F. Lankford, and J. J. Reilly, Hyperfine Interactions **31**, 235 (1986).
- [62] A. Amato, H. Luetkens, K. Sedlak, A. Stoykov, R. Scheuermann, M. Elender, A. Raselli, and D. Graf, Review of Scientific Instruments **88**, 093301 (2017).
- [63] Note that we suspect that the sample wasn't fully thermalized during the measurement shown in Fig. 6(a). A comparison to the temperature dependence in Fig. 7 gives an effective temperature of  $\approx 13$  K.
- [64] This corresponds to an angle of  $\pm 0.5^\circ$  in  $k_y$  direction

(denoted as tilt rotation in Figure 2 of Ref. [36]) or a misalignment in the inplane rotation of  $\pm 5^\circ$ .

[65] In a transverse field ( $B_{\text{ext}}$ ) the mean field

$$B = \sqrt{(B_{\text{ext}} + B_{\perp})^2 + B_{\parallel}^2} = \sqrt{B_{\text{ext}}^2 + 2B_{\text{ext}}B_{\perp} + B_{\text{int}}^2}$$

is more sensitive to out-of-plane components ( $B_{\perp}$ ) than to in-plane components ( $B_{\parallel}$ ) of the internal magnetic field  $B_{\text{int}}$ .